Aerothermal characteristics of bleed slot in hypersonic flows

YUE LianJie[*], LU HongBo, XU Xiao & CHANG XinYu

State Key Laboratory of High Temperature Gas Dynamics, Institute of Mechanics, Chinese Academy of Sciences, Beijing 100190, China

Two types of flow configurations with bleed in two-dimensional hypersonic flows are numerically examined to investigate their aerodynamic thermal loads and related flow structures at choked conditions. One is a turbulent boundary layer flow without shock impingement where the effects of the slot angle are discussed, and the other is shock wave boundary layer interactions where the effects of slot angle and slot location relative to shock impingement point are surveyed. A key separation is induced by bleed barrier shock on the upstream slot wall, resulting in a localized maximum heat flux at the reattachment point. For slanted slots, the dominating flow patterns are not much affected by the change in slot angle, but vary dramatically with slot location relative to the shock impingement point. Different flow structures are found in the case of normal slot, such as a flow pattern similar to typical Laval nozzle flow, the largest separation bubble which is almost independent of the shock position. Its larger detached distance results in 20% lower stagnation heat flux on the downstream slot corner, but with much wider area suffering from severe thermal loads. In spite of the complexity of the flow patterns, it is clearly revealed that the heat flux generally rises with the slot location moving downstream, and an increase in slot angle from 20° to 40° reduces 50% the heat flux peak at the reattachment point in the slot passage. The results further indicate that the bleed does not raise the heat flux around the slot for all cases except for the area around the downstream slot corner. Among all bleed configurations, the slot angle of 40° located slightly upstream of the incident shock is regarded as the best.

boundary layer control, boundary layer heat flow, shock wave interactions, separated flows

PACS number(s): 47.85.ld, 44.20.+b, 47.40.Nm, 47.32.Ef

1 Introduction

Bleed systems are widely used to improve the performance of subsonic, transonic and supersonic devices such as airfoils, inlets of jet engines, wind tunnels, and frames of supersonic aircraft. For these devices, bleed systems, which extract the low momentum fluid from the boundary layer next to the solid surface, can reduce both boundary layer thickness and the severity of separation [1,2], even delay the boundary layer laminar-turbulent transition, known as laminar flow control [3]. For example, large regions of laminar flow for an aircraft can be realized in flight using slot-suction laminar flow control, leading to a pronounced reduction in drag and a remarkable improvement in fuel efficiency [3]. For transonic wings and supersonic inlets, the overall performance is significantly affected by the presence of shock wave-boundary layer interactions (SWBLIs) and boundary layer bleed can be used to reduce the adverse effects of SWBLIs [4–7]. At wind tunnels, bleed slots can be employed to maintain a laminar boundary layer on the nozzle wall and avoid acoustic fluctuations generated by boundary layer turbulence, further replicating the low noise conditions of actual flight [8].

These considerable benefits provided by bleed have led a number of investigators to explore its potentials in hypersonic devices both experimentally and numerically [9–21].

---

*Corresponding author (email: yuelj@imech.ac.cn)

Numerical and experimental investigations were conducted by Schulte et al. [9,10] to examine the influences of bleed configuration parameters on the bleed efficiency in hypersonic inlets, including bleed slot width, slot angle and slot position. The results claimed the position of bleed slot directly upstream of the shock impingement location as the most favorable. The application of a correctly designed and positioned bleed system can make a significant increase in the attainable total pressure recovery of hypersonic inlets, as well as a reduction in the separation bubble thickness. Häberle and Gülhan [11,12] deployed a passive boundary layer bleed at the throat of a fixed geometry hypersonic inlet to significantly diminish the lip shock-induced separation bubble on the ramp and reduce the risk of inlet unstart with 5% mass flow rate penalty. Falempin et al. [13], Chang et al. [14] and Pandian et al. [15] also adopted perforation bleed as an efficient method to facilitate inlet starting and improve their overall characteristics. Herrmann et al. [16] experimentally investigated the effects of different boundary layer bleed systems on the performance of a two-dimensional ramjet inlet and identified that the boundary layer bleed could significantly increase the inlet performance and stabilize the subcritical condition (i.e., later buzzing). Mitani et al. [17], Kouch et al. [18] also showed that the bleed suppressed effectively the boundary layer separation, improved the unstart characteristics in engines and doubled the engine operating range. Yue et al. [19] further explored the effectiveness of boundary layer bleed in improving the performance of a scramjet engine, and observed that the bleed should be sophisticatedly designed at an exact location. Additionally, Donbar et al. [20], and Weiss and Olivier [21] experimentally investigated the influence of boundary layer suction slot on the behavior of a shock train in an isolator. It was concluded that the back pressure of the shock train can be increased because the suction stabilized primary shock foot. The aforementioned research argues that boundary layer bleed can provide huge potential benefits for hypersonic inlets.

However, at hypersonic conditions, the mass flow passing into bleed slots or holes is heated, resulting in aerodynamic heating on the bleed walls, i.e. heat is transferred from the high temperature air to the solid surfaces. The detrimental heating can burn the surface material [22]. Also, the steep spatial difference of the heating rates can produce a large thermal stress, sharply reducing the service life of the materials [23]. Thus a critical issue is to evaluate the heat transfer rate of bleed systems for its implementation in the hypersonic inlets and the design of an appropriate thermal protection system. Nevertheless, to the authors' knowledge, few studies have been conducted to study the aerodynamic thermal loads of bleed systems. The objective of the paper is to extend earlier work to aerodynamic heating of bleed configurations. A numerical study of bleed in two-dimen- sional high enthalpy flow with and without shock impingement is conducted to extensively characterize the bleed flow phenomena and the corresponding aerody-

namic thermal loads, specially focusing on the bleed interaction region.

2 Description of flow phenomena around the bleed interaction region

Extensive investigations of bleed in supersonic flowfields with and without shock impingement have been conducted to analyze the bleed flow phenomena and its effectiveness in flow control [24–34]. Syberg and Koncsek [24] studied the effects of bleed hole size, slant angle, and length-to-diameter ratio on flow characteristics in the bleed zone without shock impingement. Hamed et al. [25,26] surveyed the oblique shock wave and laminar boundary layer interaction with bleed. Hahn et al. [27], Hamed et al. [28–30], and Davis and Willis [31] further investigated the oblique shock wave and turbulent boundary layer interaction with bleed through various normal and slanted slots. In their studies, a set of parameters were examined, including bleed mass flow rates, slot location relative to shock impingement point, slot angle, and slot length-to-width ratio. Moreover, Shih, Chyu, and Rimlinger [32–34], and Hamed et al. [35] numerically characterized three dimensional flow features in the vicinity of bleed holes with shock impingement. Through the aforementioned investigations, several important features of the bleed interaction are identified, as shown in Figure 1. The two most striking features are the presence of a separation bubble in the bleed passage and the bleed barrier shock. The separation bubble determines the aerodynamic throat of the bleed passage and has an important effect on the flow coefficient of the slot or hole. Bleed barrier shock strength plays an important role in shock wave/boundary layer interactions within the bleed passage and the boundary layer development on the plate surface downstream of the bleed zone. Whether the bleed barrier shock detaches or not depends on local flow conditions, specially the slot angle α, if the conjunction between the slot or hole and the surface parallel to the freestream flow is deemed sharp. Furthermore, more complex flow pattern occurs in the presence of incident shock. In our research, the flow characteristics are found to be different even if the bleed slot is located at a slightly different position within the interaction region. In fact, the bleed flow characteristics with shock impingement still need extensive survey. Undoubtedly, the flow patterns around the bleed would strongly affect the aerodynamic thermal loads on the bleed wall and the surface downstream of the bleed slot or hole. Unfortunately, to date, the aerodynamic heating accompanied by these bleed flow features is still unknown.

To examine the effects of the mentioned factors on aerodynamic thermal loads on the bleed wall, this paper investigates two types of flow configurations with bleed. The first type is the turbulent boundary layer flow (TBLF) on a plate with bleed, but without shock impingement. In this
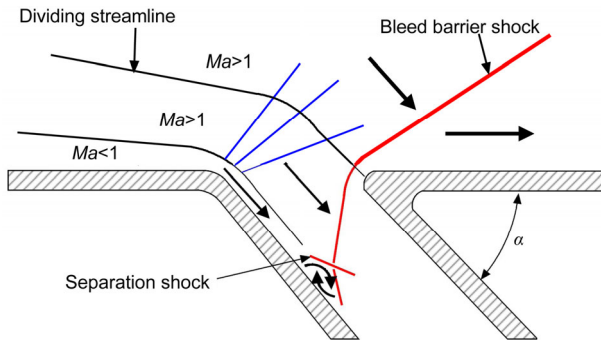
Figure 1   (Color online) Schematic of the bleed interaction region (no scale).

configuration, different slot angles are studied to analyze the effects. The second type is shock wave boundary layer interactions (SWBLIs) on a plate with bleed. In the SWBLIs configuration of previous work, the slot location relative to shock impingement point is set by the inviscid incident shock without consideration of the influences of boundary layer and bleed on the incident shock shape, leading to a void of the interference between bleed barrier shock and the incident shock. Thus different slot locations relative to the real shock impingement point are studied in the SWBLIs configuration besides bleed slot angles. Since suction within the interaction region was found to be more effective in suppressing the effects of separation, three different locations of the suction slot relative to the shock impingement point are designed within this region to analyze their influence, including the incident Shock impingement on the Upstream Slot Corner (SoUSC), the incident Shock impingement on the Slot Opening Center (SoSOC) or Downstream Slot Corner (SoDSC). The effects of the slot angle, including 20°, 30°, 40° slanted and 90° normal are investigated in this paper by referring to earlier work [29]. All the results are obtained at the condition of the bleed passage flow choked.

3   Numerical methods and computational overview

3.1   Numerical methods

The full Navier-Stokes equations for two-dimensional turbulent flow are numerically solved by the finite volume method. The convection terms of the governing equations are discretized with a second-order TVD method based on a new multi-dimensional interpolation framework. An approximate Riemann solver named Harten-Lax-van Leer contact (HLLC) is used to define interface fluxes based on local wave-model solutions. The minmod limiter is employed to suppress spurious oscillations near the discontinuities while high-order accuracy is retained away from the jumps. The time terms are discretized with a second-order fully implicit scheme. The turbulence model of k-ω SST is

employed to close the governing equations with a compressibility correction for high Mach number flows. In addition, the multi-grid and dual time-step methods are employed to accelerate convergence. Our previous studies [36,37] have verified that the adopted numerical algorithm is very credible and can efficiently resolve high Mach number flows and aerodynamic heating.

2-D incident shock wave on a flat plate turbulent boundary layer is chosen to further validate the numerical methods because SWBLI is an important phenomenon in this study [38]. The nominal test conditions are Mach number $M_0 = 5.0$, total pressure $P_t = 2.12$ MPa, total temperature $T_0 = 410$ K, wall temperature $T_w = 300$ K, with air as the working medium. The shock generator angle is 14° and the inviscid shock impingement position is 350 mm from the leading edge of the flat plate. The first normal mesh spacing at the wall is 1.0 μm with the y^+ at the surface less than 1. Figure 2 presents the Stanton number on the plate for this fully separated case. CFD results show an increase in wall heating through the separation bubble region. And numerical Stanton number agrees well with the experimental data. The numerical methods are fairly good enough to be qualified for aerodynamic heating calculation.

3.2   Computational details

Figure 3(a) shows the solution domain used in our two-dimensional simulations. It includes the region above the flat plate and inside the slot. At the inflow boundary AB, a freestream high enthalpy airflow with $T_t = 1824.5$ K, $Ma_1 = 4$, $P_1 = 22.755$ kPa and $Re = 1.071 \times 10^6$ m^{-1} is imposed, which approximately corresponds to the flow conditions in the internal contraction section of hypersonic inlets operating at flight Mach number of 6 and altitude of 26 km. Generally, bleed systems are usually installed around this section [11,17,18]. The boundary AB has a turbulent boundary layer with the streamwise velocity profile described by the van Driest profile with one-seventh power law, where the boun-
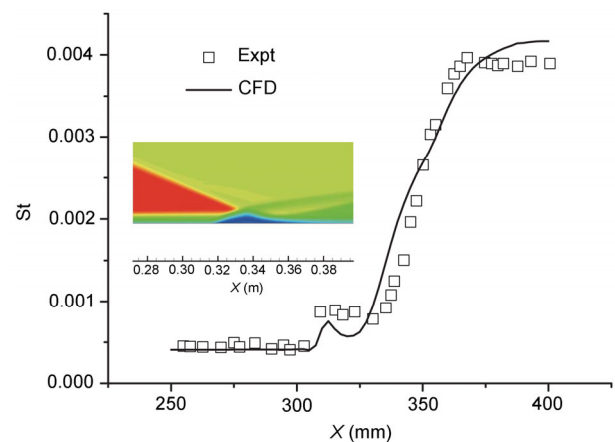

Figure 2   (Color online) Comparison between CFD and experimental Stanton number.
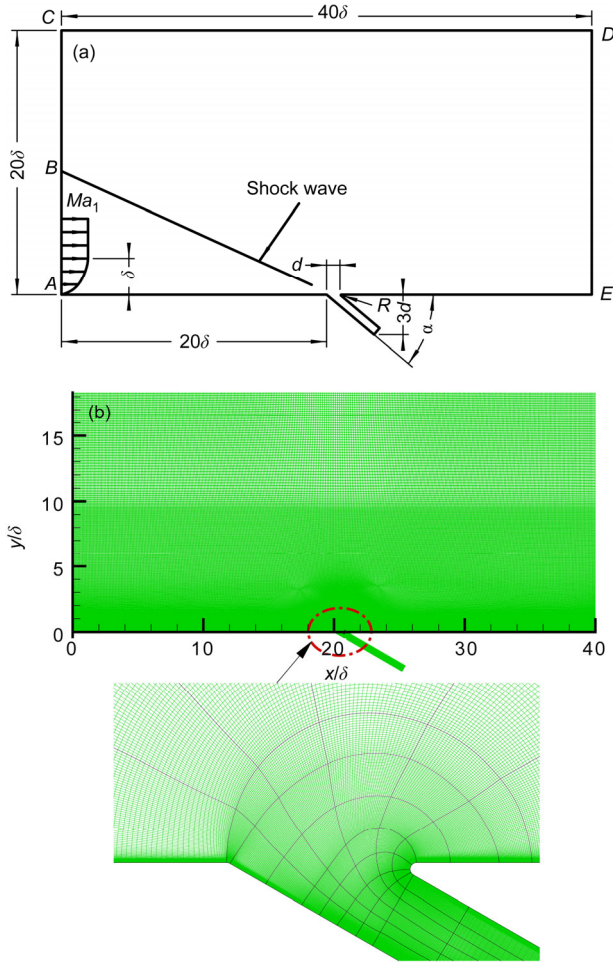
Figure 3   Schematic diagram of the bleed-slot problem studied (δ=5 mm). (a) Computational domain, (b) grid mesh distribution.

dary layer thickness δ is 5 mm. Along BC and CD, the freestream conditions are specified in the absence of shock impingement, whereas post-shock conditions based on inviscid oblique shock wave theory are specified in the presence of shock impingement. The incident shock angle β is 24.6°, at which a separation is induced by the incident shock when there is no bleed. At the outflow boundary DE, the flow is mostly supersonic except within a small region next to the wall so that all flow variables are extrapolated from interior. At all solid surfaces, the no-slip isothermal temperature conditions are applied, where $T_W = 300$ K. At the outflow boundary of the bleed slot, all flow variables are also extrapolated from interior because the bleed slot operates at choked conditions in our calculation.

To maintain comparable bleed mass among different slanted as well as normal bleed configurations, the bleed slot opening without consideration of the slot corner bluntness is kept at a fixed value [29], equal to the turbulent boundary layer thickness, i.e. $d = \delta = 5$ mm in this paper. The conjunction between the downstream slot wall and the flat plate is then blunted with a radius R of 0.2 mm to investigate the aerodynamic heating on a bleed blunted corner.

The real opening width varies a little for different slot angles. The remaining dimensions in Figure 3(a) are given in terms of δ. The angle α between the slot and the plate, together with the slot location relative to the shock impingement point, is varied to study their effects on flow characteristics and thermal loads.

Our calculations are performed on a multi-block domain with 0.21 million grids in total, as shown in Figure 3(b). To enhance the resolution of flow patterns around the bleed interaction region, H-C grid is employed and C-grid is used in the portion of the upstream and downstream slot corner. Grid stretching is specially applied in the normal direction near the solid surface. The first mesh size normal to the wall is 1 μm, corresponding to $y^+ < 1$ on the solid surface. The grid number in the turbulent boundary layer is greater than 60 so that the temperature gradient in the boundary layer can be well resolved. To ensure the convergence, the heat flux is monitored at the point 16δ downstream of the plate leading edge. When it almost reaches constant, the solution is deemed converged.

4   Numerical results and discussion

In the section, the bleed flow patterns and the aerodynamic thermal loads on the solid wall are discussed for various configurations, including those with or without incident shock, the effects of different slot angles and varied slot locations relative to the shock impingement point. In the following discussions, the aerodynamic heating on the solid surface is denoted in terms of Stanton number (St) defined

as $St = \dfrac{q_W}{\rho_1 U_1 C_p (T_t - T_W)}$,   where q_W, C_p, ρ_1, U_1, and T_t de-

notes the heat flux on the solid surface, specific heat, density, streamwise velocity, and total temperature at the inflow boundary AB, respectively.

4.1   Effects of slot angle without shock impingement

The bleed flow characteristics are demonstrated first to support the analysis of thermal load in the bleed region. Figure 4 shows Mach contours and streamlines around the bleed interaction region in TBLF for four different slot angles. An expansion fan emanates from the upstream slot corner and then a detached bleed barrier shock occurs at the downstream slot corner. Another noticeable feature is observed that a recirculation flow region inside the slot is induced by bleed barrier shock striking on the boundary layer over the upstream slot wall in all cases. The separation bubble size and the location strongly depend on the slot angle. It is found that the separation bubble size increases with the slot angle. For $\alpha = 20°$, 30°, 40°, and 90° the separation bubble length is 2.34, 3.05, 5.81, and 6.77 mm, respectively. This trend of the separation severity is mainly attributed to
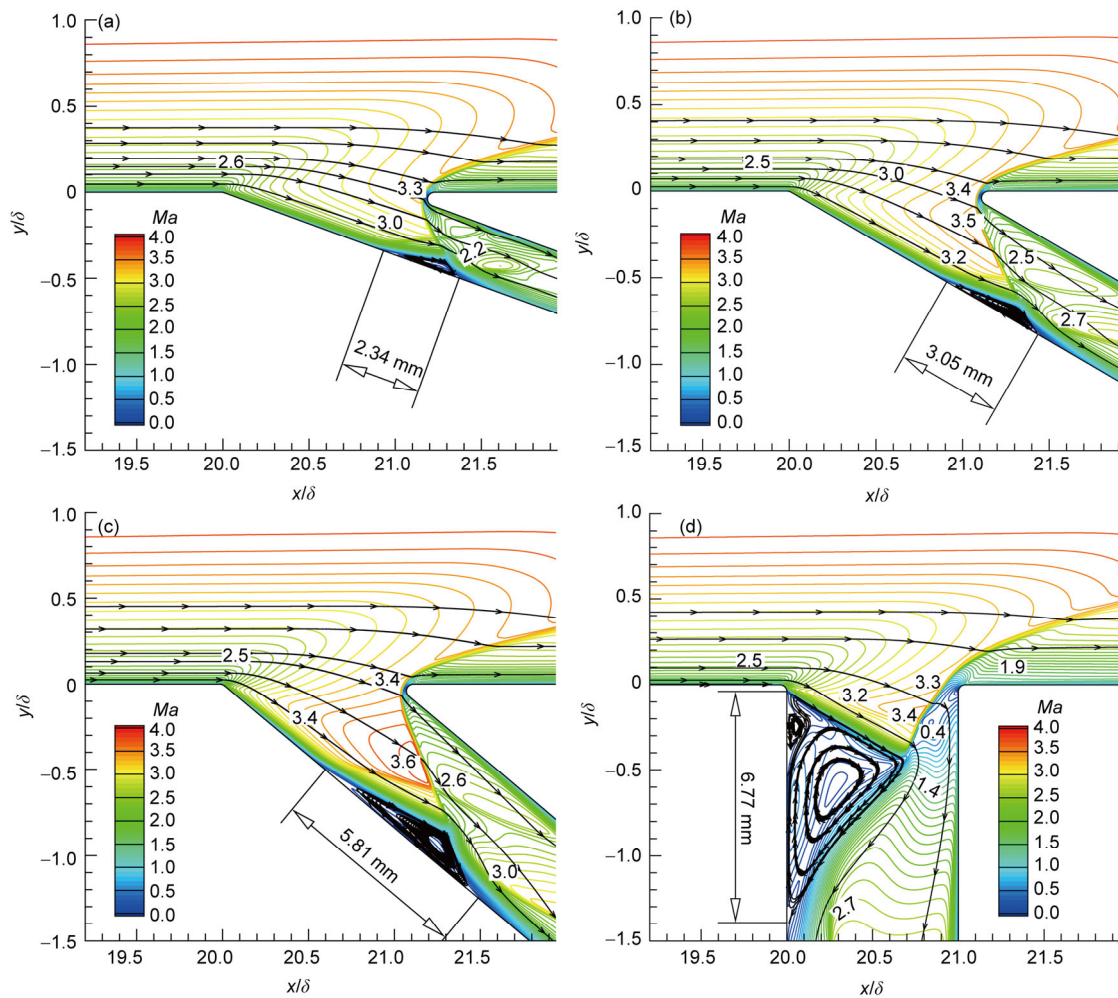
Figure 4   (Color online) Mach contours and streamlines around the bleed interaction region in TBLF. (a) $\alpha = 20°$, (b) $\alpha = 30°$, (c) $\alpha = 40°$, (d) $\alpha = 90°$.

the increases in both the intensity of bleed barrier shock and the expansion from the upstream slot corner with increasing slot angle. In addition, a secondary recirculation flow is identified at the upstream slot corner in the case of normal slot ($\alpha = 90°$).

The corresponding heat flux distributions on the upstream and downstream slot walls are presented in Figure 5. A similar tendency is observed from Figure 5(a) in the distribution of Stanton number on the upstream slot wall. The heat flux drops steeply from the upstream slot corner due to the effect of expansion fan. In the case of slanted slot, the heat flux continues to decrease with an increase in the distance from the slot corner due to the development of the boundary layer on the upstream slot wall (see Figures 4(a)–(c)) until it starts to grow within the key separation region. A local maximum heat flux is reached at the reattachment point of separation before dropping back to a lower level. In the case of normal slot, a small peak occurs at $y/\delta = -0.2$ before the reattachment point of key separation due to the effects of the secondary separation flow, as shown in Figure 4(d). Notably, contrary to the severity of

the separation shown in Figure 4, the local maximum Stanton number reduces with the increase of the slot angle. For $\alpha = 20°$, $30°$, $40°$, and $90°$, the second maximum value is 0.00123, 0.00065, 0.000537, and 0.000538, respectively. The heat flux peak for $\alpha = 30°$ drops to almost half of that for $\alpha = 20°$. This trend results from the difference in pressure at the reattachment point. Neumann suggested a relation between maximum pressure in the interaction p_{max}, maximum heating q_{max} for shock wave/boundary layer interactions as follows: $q_{max} \propto p_{max}^{n}$ [39]. For four cases in Figure 4, the incoming flow conditions upstream the slots are nearly identical. Hence the pressure at the reattachment point dominates its heat flux in spite of flow complexity in the bleed passage. For $\alpha = 20°$, $30°$, $40°$, and $90°$, the pressure at the reattachment point is 17, 9.55, 7.27, and 7.45 kPa, respectively. It reduces with the increase of the slanted slot angle due to larger expansion, but it change little between $\alpha = 40°$ and $90°$. Corresponding Stanton number shows the same trend as the pressure.

As shown in Figure 5(b), the heat flux distribution on the downstream slot wall with slanted slot differs dramatically
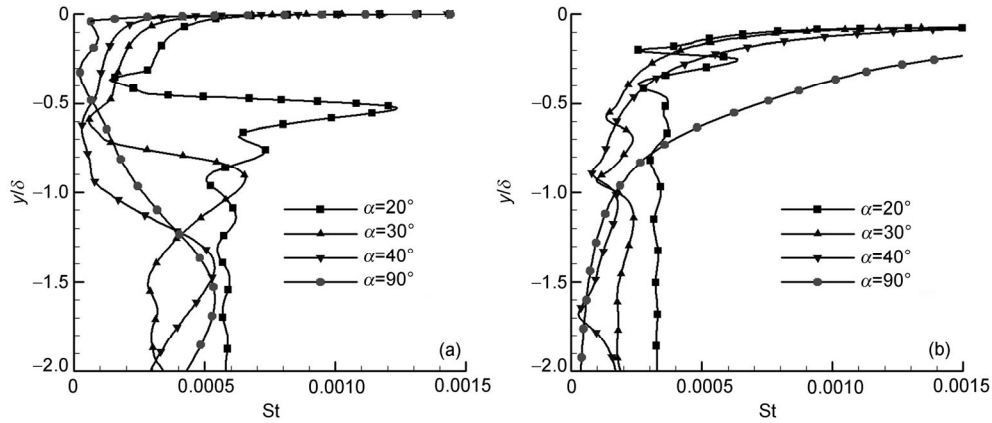
Figure 5   Stanton number distributions on the slot wall in TBLF. (a) Upstream slot wall, (b) downstream slot wall.

from the one with normal slot. Obviously, the heat flux reaches the maximum value at the stagnation point of the blunted corner. For $\alpha = 20°$, 30°, 40°, and 90°, the corresponding stagnation Stanton number is 0.0156, 0.0143, 0.0144, and 0.0111 respectively, which are not plotted yet because of the scale limit of abscissa. The stagnation heat flux for normal slot is about 25% lower than those for slanted slots. The difference is attributed to the different detachment mechanism of bleed barrier shock, which makes the detached distance much larger for the normal slot, as shown in Figure 4. The corresponding Mach number and flow angle distributions across the slot opening in Figure 6 demonstrate that the detachment mechanism of bleed barrier shock is essentially different for slanted and normal slots. Figure 6(a) illustrates that the Mach number approximates to 3.5 in the vicinity of the downstream slot corner in all the cases, whose maximum flow deflection angle is about 36.87° for the oblique shock wave being attached. Figure 6(b) shows the flow direction in the vicinity of the downstream slot corner. Flow angle is about 16° for $\alpha = 20°$ and about 20° for other cases, indicating that the corresponding angle between the local flow and the slot wall is 4°, 10°, 20°, and 70°, respectively. Thus for slanted slots ($\alpha = 20°$, 30°,

and 40°), the detachment shock is induced due to the slot corner bluntness. Whereas for normal slot ($\alpha = 90°$), it is caused by too large flow deflection angle, i.e. the angle between the local flow and the downstream slot wall exceeds the maximum deflection angle corresponding to the local Mach number, resulting in a larger detached distance. Note that, the stagnation heat flux is much larger than that on the plate without bleed (0.0013) though it can be lowered with an increase in the blunted radius. Hence, the necessity of practical bleed design should be evaluated cautiously.

With an increase in the distance from the slot corner, the heat flux on the downstream slot wall fluctuates to reduce in the case of slanted slot, while exponentially reduces in the case of normal slot. The supersonic flow dominates in the case of slanted slot and a series of SWBLIs resulting from shock reflections trigger local peaks and the fluctuation of St. However, in the case of normal slot, the flow pattern is similar to a typical Laval nozzle flow. Within the region close to the blunted corner, the subsonic flow with higher static temperature exerts much severer thermal load than those in the case of slanted slot. St reduces continuously with flow acceleration downstream of the aerodynamic throat. Further, larger slot angle contributes to lower St.
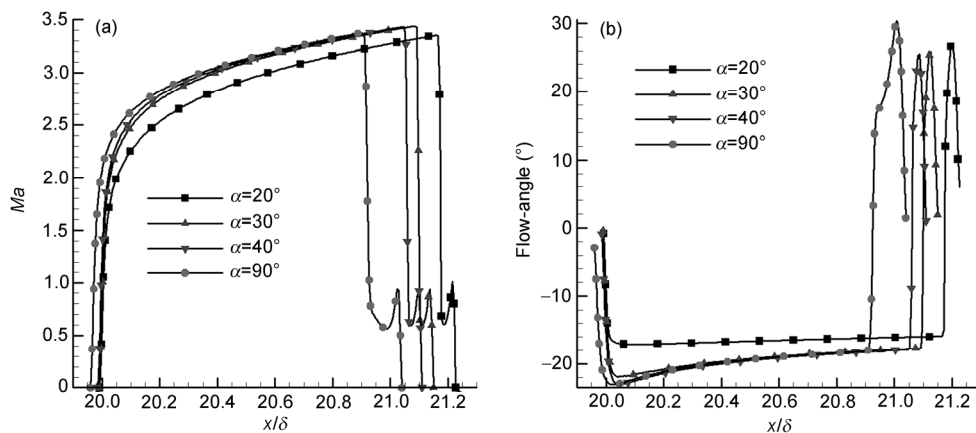

Figure 6   Distributions of Mach number and flow angle across the slot opening in TBLF. (a) Mach number, (b) flow angle.

Further insight can be gained from the heat flux distributions on the plate downstream of the slot in Figure 7. It can be seen that a sharp reduction occurs in the heat flux on the plate downstream of the slanted slot and then a local peak is reached before gently declining. For normal slot, the local heat flux peak cannot be identified within the numerical domain. These different heat flux distributions indicate that the boundary layer on the plate downstream of slanted slot quickly recovers to redevelop, whereas the one with normal slot develops with a strong entropy gradient because of different shock detachment mechanism and the stagnation point behind the bow shock slightly inside the downstream slot wall. Generally, the Stanton number is very close to that without bleed for any slot angle.

4.2   Effect of slot location relative to shock impingement point

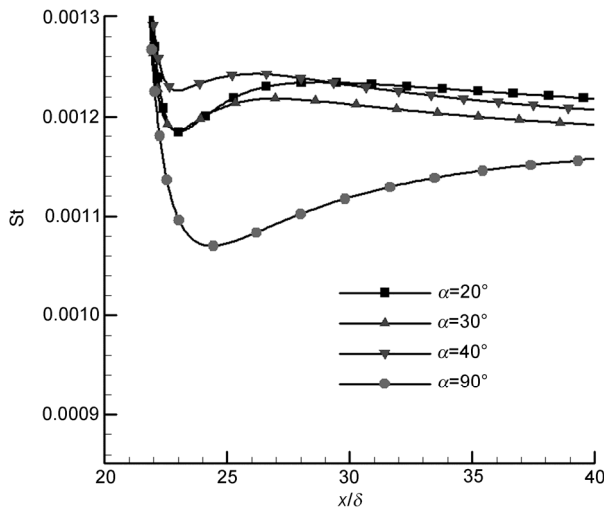Figure 8 presents the flowfield in the oblique shock wave boundary layer interactions without bleed and the corre-sponding Stanton number distribution on the plate, where the flow deflection angle is 12.5°. A separation with its length equal to 1.9δ occurs in the vicinity of the oblique shock impingement location, as shown in Figure 8(a), leading to a sharp increase in Stanton number at the reattachment location shown in Figure 8(b). The Stanton number at the reattachment position is 0.007, which is about 5.3 times of that at the point in front of the separation region.

Figure 9 presents flow patterns around the bleed interaction region for different slot locations relative to the shock impingement point in the case of $\alpha = 30°$. Compared with Figure 8, it is found that the induced separation bubble is completely eliminated by bleed for all configurations, and the bleed barrier shock above the plate merges into the reflection shock. However, it is further revealed that the shock impingement location has a crucial influence on flow patterns around the bleed interaction region. For an incident Shock impinging on the Upstream Slot Corner (SoUSC), as plotted in Figure 9(a), a very small separation occurs at the incident shock impingement location and a weak shock wave reflects. Another large separation bubble is also observed on the upstream slot wall. By contrast with the case without shock impingement shown in Figure 4(b), the separation bubble size decreases since weaker barrier shock results from flow downward deflection across the incident shock. At the incident Shock impinging on the Slot Opening Center (SoSOC), the separation bubble extends to the upstream slot expansion corner, as shown in Figure 9(b), leading to a remarkable reduction in the aerodynamic slot opening. This can be attributed to coupling effects of the incident shock and the barrier shock. At the incident Shock impingement on the Downstream Slot Corner (SoDSC), the incident oblique shock intersects the strong portion of the bow bleed barrier shock, leading to shock-on-shock interaction shown in Figure 9(c). A type III+ shock interference pattern from Edney's definition [40] occurs and then the distorted barrier shock forms in the slot passage. The severe separation with a length of 4.99 mm causes a complicated structure involving three shocks and a shear layer. It can be
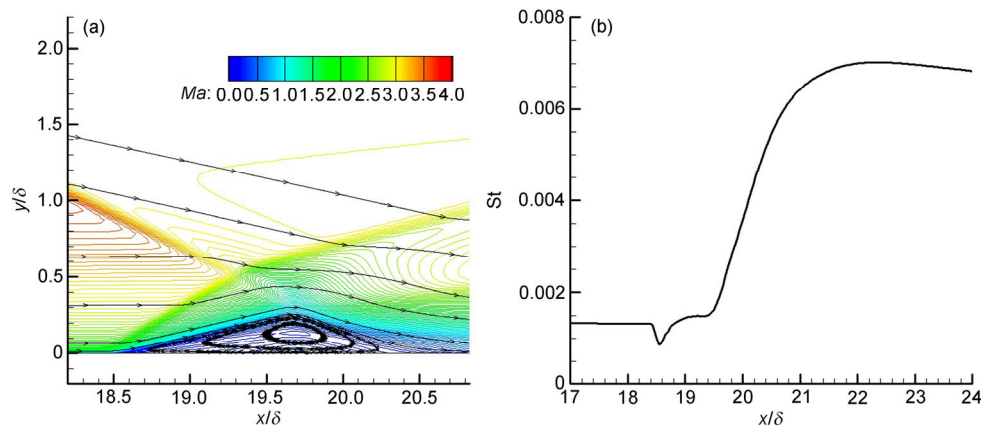

Figure 7   Stanton number distributions on the plate downstream of the bleed slot in TBLF.

Figure 8   (Color online) SWBLIs on a flat plate without bleed. (a) Computational domain, (b) Stanton number distribution.

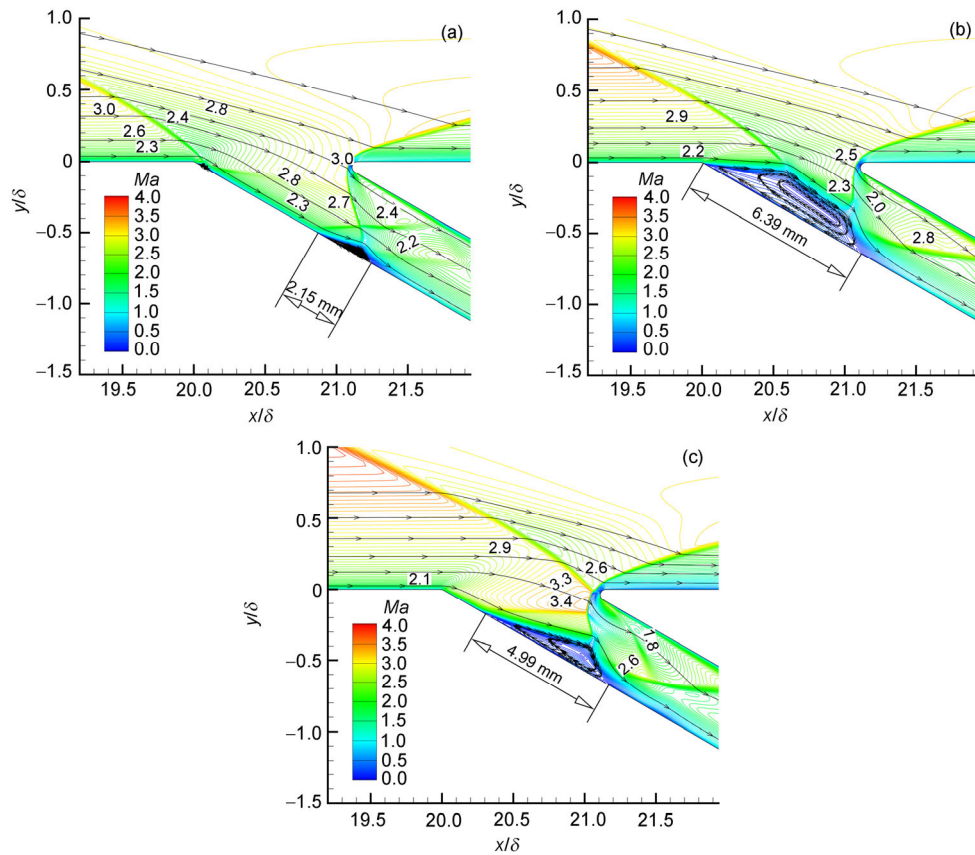**Figure 9**   (Color online) Effects of slot location relative to shock impingement point on flow patterns for $\alpha = 30°$. (a) Shock on Upstream Slot Corner, (b) Shock on Slot Opening Center, (c) Shock on Downstream Slot Corner.

inferred that a maximum heat flux exists in the key separation size when the shock impingement location moves from the upstream to the downstream slot corner for $\alpha = 30°$.

For $\alpha = 90°$, the influence of slot location relative to shock impingement point on bleed flow patterns are presented in Figure 10. It is revealed that the shock impingement location has little influence except on the bleed barrier shock. No matter where the incident shock impinges or whether there is an incident shock or not, the flow patterns in the slot are almost identical. Similar to Figure 4, a large scale separation is produced, accompanied by a small second anticlockwise recirculation flow. These separation sizes are not far different from each other for all configurations, 6.63 mm at SoUSC, 5.77 mm at SoSOC, and 6.43 mm at SoDSC. Due to shock-on-shock interactions at SoDSC, a type II⁺ shock interference pattern occurs, and a convergent-divergent streamtube forms between the plate and the shear layer emanating from the intersection point between the incident and the distorted bleed barrier shocks. Undoubtedly, shock interference pattern depends on the location of the intersecting point relative to the barrier bow shock. Anyone among the six types of shock interference patterns can occur with a change in the location of the downstream slot corner.

The effects of slot location relative to shock impingement point on the heat flux over the upstream and the downstream slot walls are shown in Figures 11 and 12. Compared with those without shock impingement shown in Figure 5, the incident shock hardly causes an essential change in the heat flux distribution on two slot walls except higher value than that without shock impingement. A little difference exists in the heat flux on the slot walls for three cases with $\alpha = 30°$ because of different separation positions and associated change in the locations of separation shock and reattachment shock. As shown in Figure 11(a), the heat flux on the upstream slot wall at SoDSC first decreases with the boundary layer development until it starts to increase within the separation bubble. But the incident shock reflection over the upstream slot wall at SoUSC triggers a rapid increase in the heat flux. At SoSOC, the heat flux immediately increases after sharp drop due to the expanded separation. Furthermore, it is clear that the heat flux generally rises with the slot location moving downstream relative to shock impingement point. This trend is attributed to higher pressure inside the passage that results from more bled flow turning into the slot. The pressure at the reattachment point is 14.25, 31.1, 42.7 kPa, with bled mass rate of 0.059, 0.108, 0.219 kg s⁻¹ per meter width, for SoDSC, SoSOC, SoUSC,
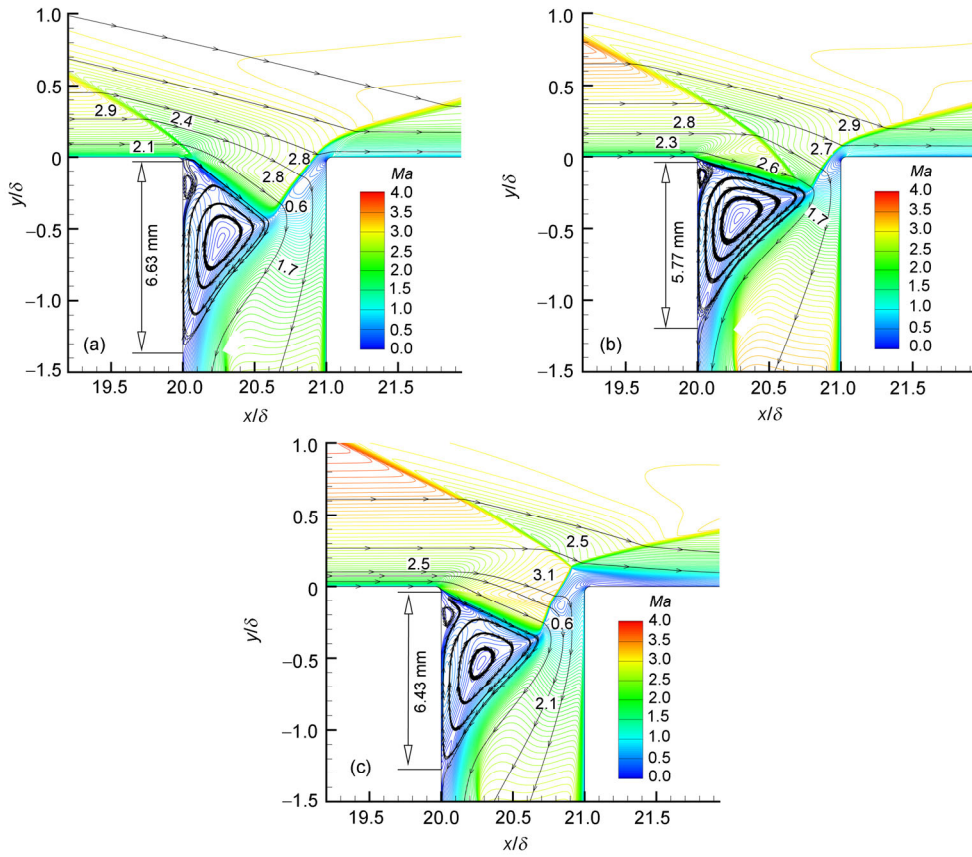
Figure 10 (Color online) Effects of slot location relative to shock impingement point on flow patterns for $\alpha = 90°$. (a) Shock on Upstream Slot Corner, (b) Shock on Slot Opening Center, (c) Shock on Downstream Slot Corner.
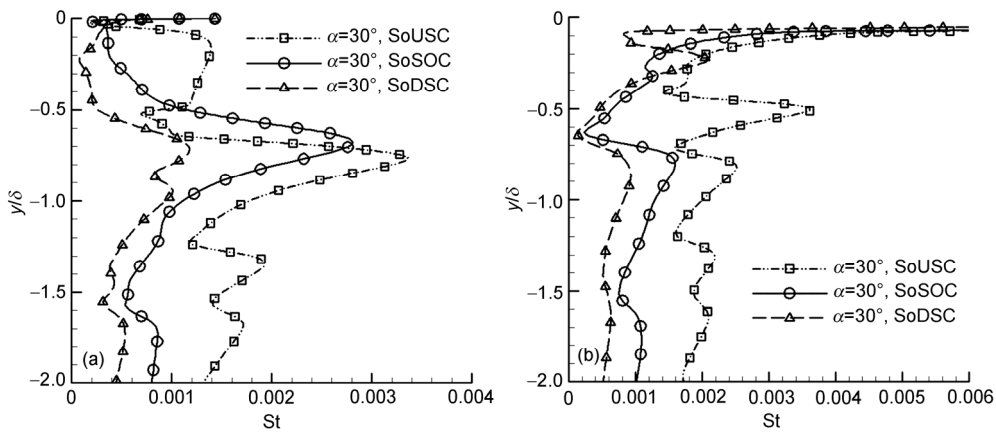

Figure 11 Stanton number distributions on the slot wall for different slot locations relative to shock impingement point with $\alpha=30°$. (a) Upstream slot wall, (b) downstream slot wall.

respectively. So the aerodynamic heat flux rises with the increase in pressure and mass flow rate. In addition, more bled flow leads to higher flow Mach number close to the downstream blunted corner, which is associated with increasing stagnation heat flux. The Stanton number at the stagnation point on the downstream slot corner for $\alpha = 30°$ is 0.0387 at SoUSC, 0.0309 at SoSOC while 0.0275 at SoDSC. And for $\alpha = 90°$ it is 0.0311 at SoUSC, 0.0240 at SoSOC while 0.0095 at SoDSC. According to the research on shock interference [37,40], the Stanton number at the stagnation point may rise dramatically at SoDSC, even higher than that at SoSOC or SoUSC, once the type IV shock interference triggers strong supersonic jet for an appropriate location of incident shock intersecting point rela-

tive to the barrier shock.

Figure 13 plots the heat flux distribution on the plate downstream of the slot for different slot locations relative to shock impingement point. A sharp reduction occurs first for all configurations, followed by a local peak before gently declining. The Stanton numbers are almost identical far downstream of the slot, also close to that without bleed. For $\alpha = 30°$, the heat flux in the downstream vicinity of the slot increases as the slot location moves downstream relative to the shock impingement point. For normal slot, as illustrated in Figure 13(b), an exception occurs at SoDSC that its local heat flux peak is higher than that at SoUSC or SoSOC. It is produced by the shear layer impingement on the surface shown in Figure 10(c) and then a rapid reduction is observed. Nevertheless, the local heat peak for all configurations is less than the heat flux at the reattachment point without bleed.

4.3   Effects of slot angle with shock impingement

Figures 14–16 further illustrate the flow patterns around the bleed interaction region for slot angle of 20° and 40° at

SoUSC, SoSOC and SoDSC, respectively. Combined with Figures 9 and 10, it can be noted that the change in slot angles does not alter the dominating flow patterns for slanted slots, but gives rise to a slight difference in the detailed flow structure, especially for $\alpha=20°$. In the case of normal slot, a large separation accompanied by a second counter-clockwise separated flow can be identified, which is different from those for slanted slots. Notably, different from that in TBLF without shock impingement shown in Figure 4, the separation bubble size does not increase monotonously with the slot angle because of the effect of incident shock.

At SoUSC, compared to Figures 4(b) and (c), the key separation bubble size decreases for 30°, and 40° because weaker barrier shock results from flow downward turning across the incident shock. Whereas, the separation bubble for $\alpha = 20°$ becomes larger. Two mechanisms lead to an irregular reflection of bleed barrier shock on the upstream slot wall. First, the Mach number of the flow turning into bleed slot for $\alpha = 20°$ is much lower through a deceleration of both the incident shock and the reflection shock wave. In addition, the local bow bleed barrier shock striking on the
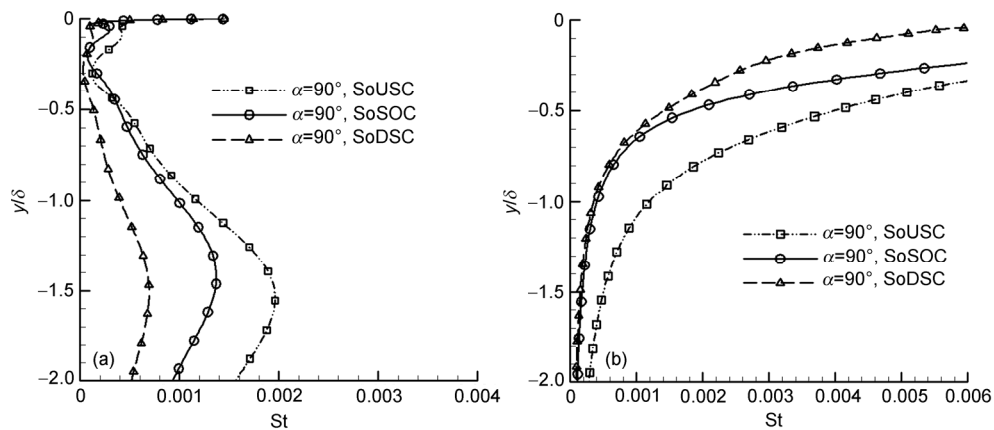

Figure 12   Stanton number distributions on the slot wall for different slot locations relative to shock impingement point with $\alpha=90°$. (a) Upstream slot wall, (b) downstream slot wall.
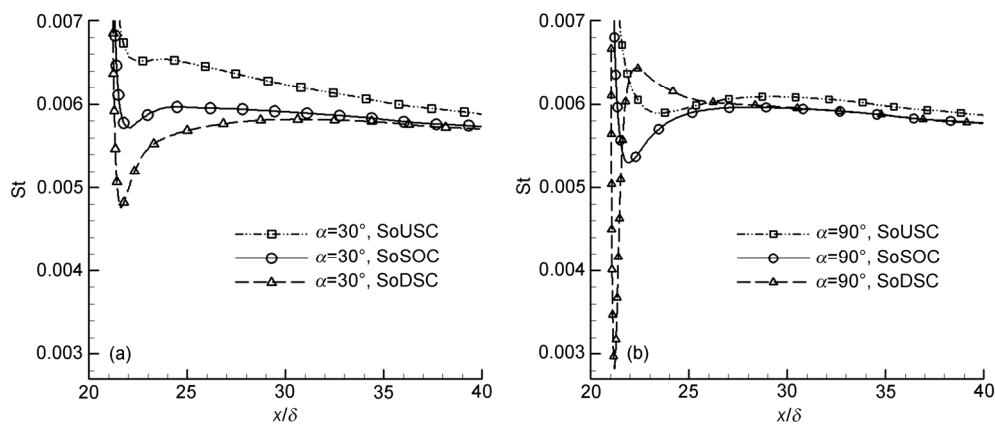

Figure 13   Stanton number distributions on the plate downstream of the slot for different slot locations relative to shock impingement point. (a) Slot angle of 30°, (b) slot angle of 90°.
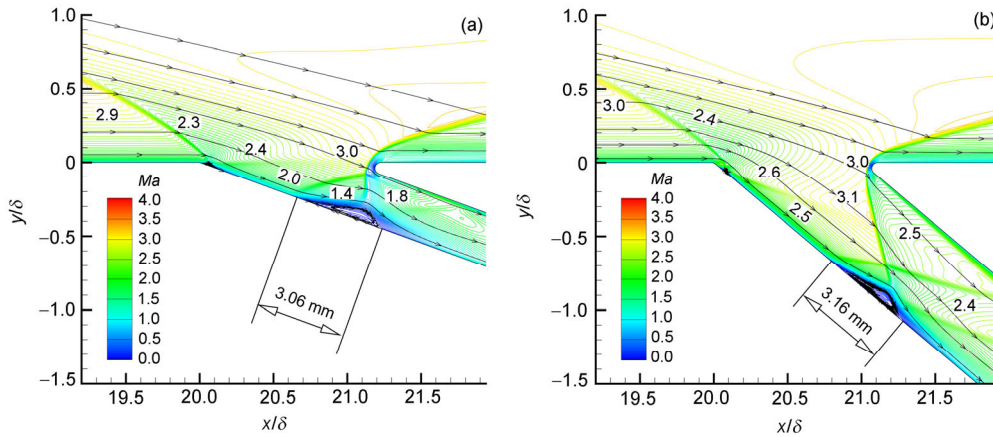
Figure 14   (Color online) Flow patterns for slot angle of 20° and 40° at SoUSC. (a) $\alpha = 20°$, (b) $\alpha = 40°$.
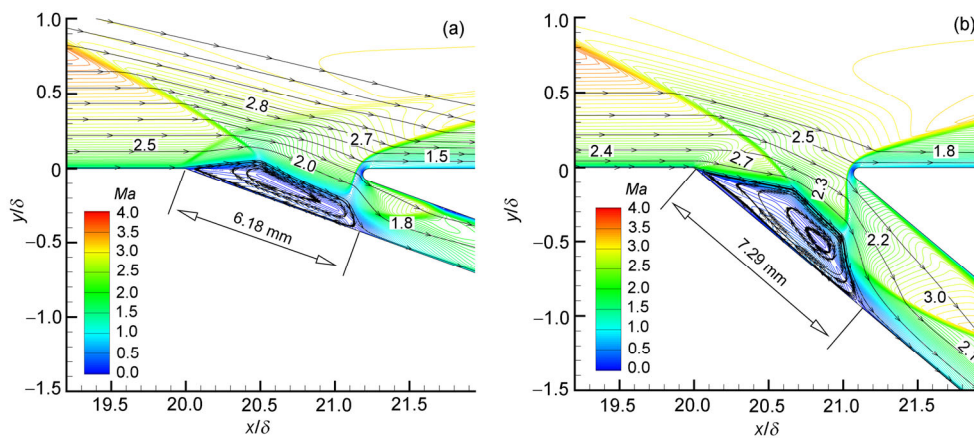

Figure 15   (Color online) Flow patterns for slot angle of 20° and 40° at SoSOC. (a) $\alpha = 20°$, (b) $\alpha = 40°$.

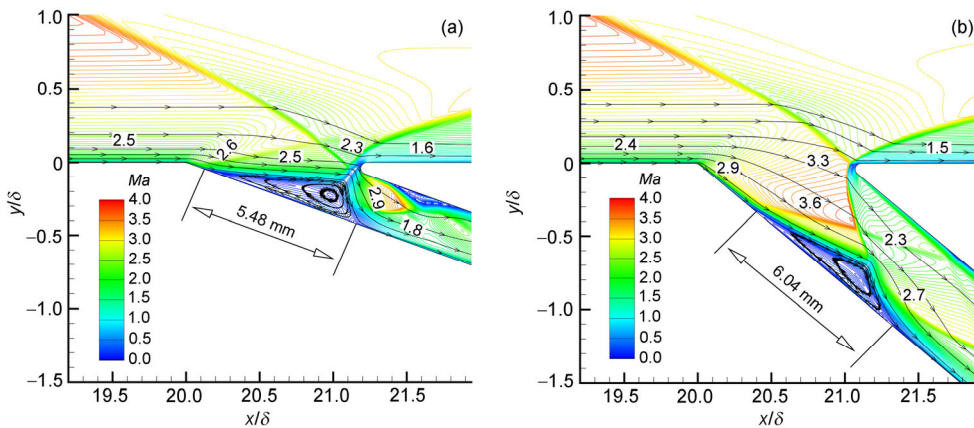**Figure 16**   (Color online) Flow patterns for slot angle of 20° and 40° at SoDSC. (a) $\alpha = 20°$, (b) $\alpha = 40°$.

surface is stronger due to a narrower bleed passage. With a larger boundary layer separation, a strong separation shock interferes with the bow bleed barrier shock, leading to a λ shock structure followed by a sonic throat downstream.

At SoSOC, the joint impact of the incident and the barrier shocks results in a large scale separation starting at the

upstream slot corner for all slanted slots. A weak shock is produced at the upstream slot corner for $\alpha = 20°$ while expansion fan emanates for larger slot angle. It can be seen that the slot angle does not alter the separation bubble size too much. At SoDSC, more complex flow pattern is created by the interference between the incident and the barrier

shocks. The shock interference varies with the slot angle because the downstream blunted corner is located slightly different. Compared to that without shock impingement shown in Figure 4, the distorted barrier shock results in a larger separation bubble for slanted slots. And the SWBLi becomes more intense with decreasing slot angle (i.e. narrower bleed passage). In particular, the barrier shock with $\alpha=20°$ triggers an irregular reflection and exhibits the flow pattern of a normal shock followed by a sonic throat and a large separation.

The corresponding heat flux distributions on the upstream and the downstream slot walls at SoUSC, SoSOC and SoDSC are presented in Figures 17–19. In a word, the effect of slot angle on the heat flux distributions for all cases is similar to that without shock impingement. A local heat peak occurs at the reattachment point of separation on the upstream slot wall, and the heat flux on both slot walls fluctuates due to the shock reflections except for normal slot. As with those without shock impingement, the heat flux in the bleed passage reduces with the increase of slot angle except on the surface close to downstream blunted corner, though the separation bubble does not grow monotonously. Also, a local maximum occurs in the Stanton number on the

plate downstream of the slot before gently reducing to about 0.0053–0.0057, which is not presented in figures. Compared to the case without shock impingement, the stagnation heat flux at downstream slot corner remarkably grows due to incident shock compression. For instance, the stagnation Stanton number for $\alpha = 20°$, $30°$, $40°$, and $90°$ increases about 1.5 times, being respectively 0.0413, 0.0387, 0.0391, and 0.0311 at SoUSC. Different detachment mechanism of bleed barrier shock makes the detached distance much larger in the case of normal slot, contributing to a 20% lower stagnation thermal load.

In sum, the bleed configuration alters the flow patterns and the associated heat flux on the surfaces around the bleed region. No matter where the slot locates or how large is the slot angle, the heat flux around the slot is lower than that without bleed, except on the surfaces around the downstream slot corner. Nevertheless, the downstream corner will face the challenge of severe thermal loads, which asks the designers to balance the benefit of the bleed and its negative effects. Of all bleed configurations, the slot angle of $40°$ located slightly upstream of the incident shock is regarded as the best in terms of the thermal loads. Its stagnation heat flux is 20% higher than that for $\alpha = 90°$, but only
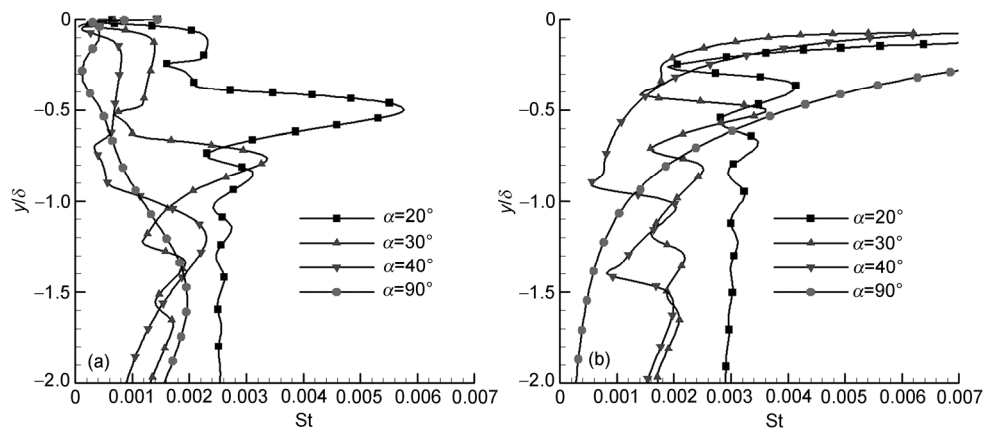

Figure 17   Stanton number distributions on the slot wall at SoUSC. (a) Upstream slot wall, (b) downstream slot wall.
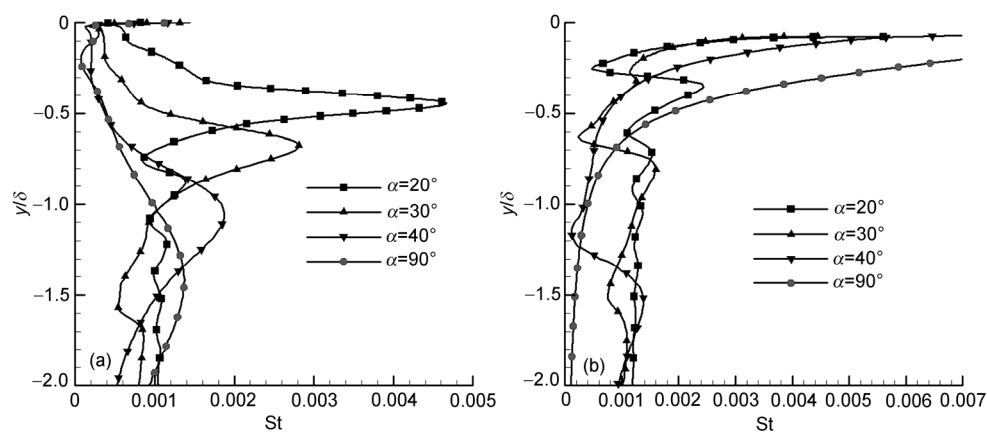

Figure 18   Stanton number distributions on the slot wall at SoSOC. (a) Upstream slot wall, (b) downstream slot wall.
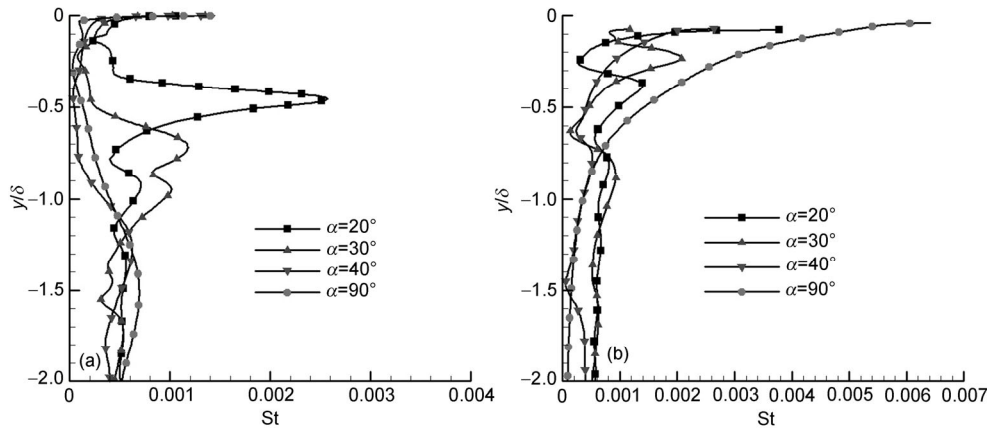
Figure 19   Stanton number distributions on the slot wall at SoDSC. (a) Upstream slot wall, (b) downstream slot wall.

the blunted corner would suffer from a high thermal load rather than much wider area in the case of normal slot. Meanwhile, its heat flux peak in the slot passage is only half of that for $\alpha = 20°$.

5   Conclusions

A numerical study is conducted to investigate the aerodynamic thermal loads of bleed systems in high enthalpy flows. Two types of flow configurations with bleed are examined. One is the turbulent boundary layer flow (TBLF) on the plate without shock impingement. And the other is shock wave boundary layer interactions (SWBLIs) on the plate. The effects of the slot angle and the slot location relative to shock impingement point are discussed at choked conditions.

A key separation is induced by bleed barrier shock striking on the boundary layer over the upstream slot wall, resulting in a localized maximum heat flux at the reattachment point. In the case of slanted slots, the change in slot angle does not alter the dominating flow patterns and heat flux distributions for the configurations with or without incident shock. A clear tendency is observed that an increase in slot angle reduces the heat flux on the slot walls except the surface close to the downstream slot corner. But in the case of normal slot, different detachment mechanism of barrier shock (i.e. too large flow deflection angle) produces larger detached distance with a somewhat typical Laval nozzle flow inside the bleed passage. These flow phenomena result in 20% lower stagnation heat flux on the downstream slot corner compared with slanted slots, but much wider area would suffer from severe thermal loads within the subsonic flow region.

The flow patterns around the bleed interaction region are strongly influenced by the slot location relative to shock impingement point in the case of slanted slot, and a maximum heat load occurs in the key separation size. In the case

of normal slot, flow structures around the bleed passage are almost independent of the slot location except that a shock interference pattern would occur at SoDSC instead of the bow bleed barrier shock. However, no matter what slot angle it is, the heat flux generally rises with the slot location moving downstream relative to the shock impingement point.

The result also indicates that the bleed does not raise the heat flux around the slot for all cases, except on the surfaces around the downstream slot corner. Nevertheless, the downstream corner will face the challenge of most severe thermal loads. Among all bleed configurations, the slot angle of 40° located slightly upstream of the incident shock is regarded as the best in terms of the thermal loads. The present study provides some insight into the flow with bleed and offers helpful references for the design of bleed systems from the viewpoint of thermal protection.

1   Ball K O W. Further results on the effects of suction on boundary layer separation. AIAA J, 1970, 8: 374–375

2   Ball K O W, Korkegi R H. An investigation of the effect of suction on hypersonic Laminar boundary-layer separation. AIAA J, 1968, 6: 239–243

3   Ronald D J. Aircraft laminar flow control. Annu Rev Fluid Mech, 1998, 30: 1–29; Deng B Q, Xu C X, Huang W X, et al. Effect of active control on optimal structures in wall turbulence. Sci China-Phys Mech Astron, 2013, 56: 290–297

4   Babinsky H, Ogawa H. SBLI control for wings and inlets. Shock Waves, 2008, 18: 89–96

5   Slater J W, Saunders J D. Modeling of fixed-exit porous bleed systems for supersonic inlets. J Propul Power, 2010, 26: 193–202

6   Ryu K J, Lim S, Song D J. A computational study of the effect of angles of attack on a double-cone type supersonic inlet with a bleeding system. Comput Fluids, 2011, 50: 72–80

7   Delery J. Shock-wave/turbulent boundary-layer interaction and its control. Prog Aerosp Sci, 1985, 22: 209–280

8   Aradag S, Knight D D, Schneider S P. Bleed lip geometry effects on the flow in a hypersonic wind tunnel. AIAA J, 2006, 44: 2133–2136

9   Schulte D, Henckels A, Wepler U. Reduction of shock induced

boundary layer separation in hypersonic inlets using bleed. Aerosp Sci Technol, 1998, 2: 231–239

10 Schulte D, Henckels A, Neubacher R. Manipulation of shock/ boundary-layer interactions in hypersonic inlets. J Propul Power, 2001, 17: 585–590

11 Häberle J, Gülhan A. Internal flowfield investigation of a hypersonic inlet at Mach 6 with bleed. J Propul Power, 2007, 23: 1007–1017

12 Häberle J, Gülhan A. Experimental investigation of a two-dimensional and a three-dimensional scramjet inlet at Mach 7. J Propul Power, 2008, 24: 1023–1034

13 Falempin F, Goldfeld M A, Semenova Y V, et al. Experimental study of different control methods for hypersonic air inlets. Thermophys Aeromech, 2008, 15: 1–9

14 Chang J T, Yu D R, Bao W, et al. Effects of boundary layers bleeding on unstart/restart characteristics of hypersonic inlets. Aeronaut J, 2009, 113: 319–327

15 Pandian S, Jose J, Patil M M, et al. Hypersonic air-intake performance improvement through different bleed systems. In: Proceedings of XV International Symposium on Air-breathing Engines. Bangalore: International Society for Air Breathing Engines, 2001. ISABE-2001-1039

16 Herrmann D, Blem S, Gülhan A. Experimental study of boundary-layer bleed impact on ramjet inlet performance. J Propul Power, 2011, 27: 1186–1195

17 Mitani T, Sakuranaka N, Tomioka S, et al. Boundary-layer control in mach 4 and mach 6 scramjet engines. J Propul Power, 2005, 21: 636–641

18 Kouch T, Mitani T, Masuya G. Numerical simulations in scramjet combustion with boundary-layer bleeding. J Propul Power, 2005, 21: 642–649

19 Yue L J, Xu X K, Chang X Y. Theoretical analysis of effects of boundary layer bleed on scramjet thrust. Sci China-Phys Mech Astron, 2013, 56: 1952–1961

20 Donbar J M, Brown M S, Linn G J. Simultaneous high-frequency pressure and TDLAS measurements in a small-scale axisymmetric isolator with bleed. AIAA Paper, 2012, AIAA-2012-0331

21 Weiss A, Olivier H. Behaviour of a shock train under the influence of boundary-layer suction by a normal slot. Exp Fluids, 2012, 52: 273–287

22 Zhao J S, Gu L X, Ma H Z. A rapid approach to convective aeroheating prediction of hypersonic vehicles. Sci China Tech Sci, 2013, 56: 2010–2024

23 Yang Q Q, Gao C F. Thermal stresses around a circular inclusion with functionally graded interphase in a finite matrix. Sci China-Phys Mech Astron, 2014, 57: 1927–1933

24 Syberg J, Koncsek J L. Bleed system design technology for supersonic inlets. AIAA Paper, 1972, AIAA-72-1138

25 Hamed A, Lehnig T. An investigation of oblique shock/boundary-layer bleed interaction. J Propul Power, 1992, 8: 418–424

26 Hamed A, Lehnig T. Effect of bleed configuration on shock/laminar boundary-layer interactions. J Propul Power, 1995, 11: 42–48

27 Hahn T O, Shih T I P, Chyu W J. Numerical study of shock-wave/ boundary-layer interactions with bleed. AIAA J, 1993, 31: 869–876

28 Hamed A, Shih S H, Yeuan J J. Investigation of shock/turbulent boundary-layer bleed interactions. J Propul Power, 1994, 10: 79–87

29 Hamed A, Yeuan J J, Shih S H. Shock-wave/boundary-layer interactions with bleed. Part 1: Effect of slot angle. J Propul Power, 1995, 11: 1231–1235

30 Hamed A, Yeuan J J, Shih S H. Shock-wave/boundary-layer interactions with bleed. Part II: Effect of slot location. J Propul Power, 1995, 11: 1236–1241

31 Davis D O, Willis B P. Flowfield measurements inside a boundary-layer bleed slot. AIAA J, 1996, 34: 1977–1983

32 Shih T I P, Rimlinger M J, Chyu W J. Three-dimensional shock-wave/boundary-layer interactions with bleed. AIAA J, 1993, 31: 1819–1826

33 Chyu W J, Rimlinger M J, Shih T I P. Control of shock-wave/ boundary-layer interactions by bleed. AIAA J, 1995, 33: 1239–1247

34 Rimlinger M J, Shih T I P, Chyu W J. Shock-wave/boundary-layer interactions with bleed through rows of Holes. J Propul Power, 1996, 12: 217–224

35 Hamed A, Morell A, Bellamkonda G. Three-dimensional simulations of bleed-hole rows/ shock-wave/turbulent boundary-layer interactions. AIAA Paper, 2012, AIAA-2012-0840

36 Lu H B, Yue L J, Xiao Y B, et al. Interaction of isentropic compression waves with a bow shock. AIAA J, 2013, 51: 2474–2484

37 Lu H B, Yue L J, Chang X Y. Flow characteristics of hypersonic inlets with different cowl-lip blunting methods. Sci China-Phys Mech Astron, 2014, 57: 741–752

38 Schulein E. Skin-friction and heat flux measurements in shock/ boundary-layer interaction flows. AIAA J, 2006, 44: 1732–1741

39 Anderson J D. Hypersonic and High Temperature Gas Dynamics. Reston: American Institute of Aeronautics and Astronautics, 2000. 301–334

40 Edney B E. Anomalous heat transfer and pressure distributions on blunt bodies at hypersonic speeds in the presence of an impinging shock. FFA Report. Stockholm: Astronautics Research Institute of Sweden, 1968. 115